North Atlantic Ocean-Originated Multicentennial Oscillation of the AMOC: A Coupled Model Study

Kunpeng Yang[1,2], Haijun Yang*[1,2], Yang Li[3], and Qiong Zhang[4]

[1]*Department of Atmospheric and Oceanic Sciences and Institute of Atmospheric Science and CMA-FDU Joint Laboratory of Marine Meteorology, Fudan University, Shanghai, 200438, China*

[2]*Shanghai Scientific Frontier Base for Ocean-Atmosphere Interaction Studies, Fudan University, Shanghai, 200438, China*

[3]*Department of Atmospheric and Oceanic Sciences, School of Physics, Peking University, Beijing, 100871, China*

[4]*Department of Physical Geography and Bolin Centre for Climate Research, Stockholm University, Stockholm, 10691, Sweden*

Journal of Climate

Submitted on July 13, 2023

Corresponding author: Haijun Yang, yanghj@fudan.edu.cn

ABSTRACT

Using a CESM1 control simulation, we conduct a follow-up study to advance our earlier theoretical research on the Atlantic meridional overturning circulation (AMOC) multicentennial eigenmode. The modeled AMOC multicentennial oscillation (MCO) is mainly contributed by internal oceanic processes in the North Atlantic, and thus can be regarded as the “North Atlantic origin” paradigm. Specifically, the AMOC MCO is primarily driven by salinity variation in the subpolar upper North Atlantic, which dominates local density variation. Salinity anomaly in the subpolar upper ocean is enhanced by the well-known positive salinity advection feedback that is realized through the perturbation circulation in the subtropical-subpolar upper ocean, and can be mixed downward and then move southward through the deep western boundary current. Meanwhile, the northward advection of salinity anomaly from the subtropical intermediate ocean through the mean circulation weakens the salinity anomaly in the subpolar upper ocean, leading to its phase change. The salinity anomalies have a clear 3-dimensional life-cycle around the North Atlantic. The mechanism and timescale of the modeled AMOC MCO are consistent with our earlier theoretical studies. Different from previous studies emphasizing the Arctic Ocean or Southern Ocean as the origin and the role of air-sea coupling, this study suggests that the AMOC MCO is more likely originated from the North Atlantic and related to internal ocean dynamics.

KEYWORDS: Coupled model, Atlantic meridional overturning circulation, Multicentennial oscillation, Salinity anomaly

1. Introduction

This work is part of our serial studies on the multicentennial oscillation (MCO) of the Atlantic meridional overturning circulation (AMOC). Our preceding studies established a theory on the AMOC multicentennial eigenmode (Li and Yang 2022; Yang et al. 2023) (hereafter LY22, YY23), and pinpointed the main processes leading to the AMOC MCO. This coupled model study is to examine whether this eigenmode exists in a complex system, to provide details on spatial structures related to the AMOC MCO in the global ocean, and to verify the theory we proposed earlier. It also presents critical clues to the AMOC MCO's origin.

Paleoclimatic proxy data from a variety of sources suggests that the Earth's climate system has variability on multicentennial timescale (Chapman and Shackleton 2000; Nyberg et al. 2002; Kim et al. 2004; Wanner et al. 2008; Newby et al. 2014; Askjaer et al. 2022). The origin and mechanism of this variability have been challenging topics for climate scientists. Previous studies suggested that the multicentennial AMOC variability is likely the driver of the multicentennial climate variability (McDermott et al. 2001; Oppo et al. 2003; Hall et al. 2004; Miettinen et al. 2012; Chabaud et al. 2014; Ayache et al. 2018; Thirumalai et al. 2018). There have been many modeling studies on the AMOC MCO using a hierarchy of models of different complexities, ranging from the simplest zero-dimensional energy balance models to coupled Earth system models. Please refer to LY22 and YY23 and references therein for a detailed review on related studies. The various AMOC MCOs in these studies might correspond to various AMOC modes on the multicentennial timescale, and do not necessarily contradict with each other. Currently, there mainly exist two problems. First, there is a lack of direct modern instrumental observations supporting variability on this timescale, which is currently insurmountable. Second, either the results obtained in simple conceptual models have not been validated by complex models, or the results from complex models have no theoretical backup. Therefore, a systematic study from simple models to complex models is necessary.

In LY22, we constructed a one-hemispheric 4-box ocean model including only salinity variation, and obtained a multicentennial eigenmode of the AMOC theoretically by further simplifying it to a 3-box model. The AMOC MCO is energized by the perturbation advection of mean salinity and dampened by the mean advection of anomalous salinity. In YY23, we progressed through including temperature variation, although at the multicentennial timescale the temperature variation in the North Atlantic was eventually found to have little impact on the AMOC MCO. At the heart of our theory is the advection processes between the subtropical and subpolar North Atlantic. This implies that this

AMOC multicentennial eigenmode can be dominated by processes in the North Atlantic, while contributions from the other oceans are not necessary. These two simple model studies improved our theoretical understanding of the AMOC MCO. However, the mechanism, the timescale, and the implied “North Atlantic origin” of this eigenmode in the simple model need to be examined thoroughly using complex models.

In an earlier coupled model study using the Kiel Climate Model (KCM), Park and Latif (2008) found an AMOC oscillation with a period of 300-400 years. Their follow-up studies, Martin et al. (2013, 2015) proposed the “Southern Ocean origin” paradigm of the AMOC MCO: when the AMOC is strong, heat content of the mid-depth water in the Weddell Sea increases due to strengthened southward transport of the warmer North Atlantic Deep Water (NADW). Deep convection in the Southern Ocean can be triggered when the heat accumulation becomes excessive, convectively releasing more heat from the deep toward the upper Weddell Sea and thus reducing the sea ice extent there. This convective cooling decreases the Atlantic north-to-south density gradient, limiting the NADW formation and thus the AMOC strength (Hughes and Weaver 1994). This is similar to the advective-convective mechanism raised by Yin (1995), that is, convection is triggered by the advective accumulation of heat. Therefore, the oscillation timescale is set by the southward advection of the NADW.

Based on a GFDL CM2.1 model simulation, Delworth and Zeng (2012) also found an AMOC MCO related to the Southern Ocean, but with a different mechanism. Starting with a weak AMOC, a positive surface salinity anomaly in the Southern Ocean can be carried northward by the upper branch of the AMOC, strengthening the NADW formation when it reaches the North Atlantic convection region, driving the AMOC into its positive phase. Synchronously, more freshwater is produced in the Southern Ocean due to the positive AMOC anomaly, and would be transported northward later. This will weaken the AMOC when the negative salinity anomaly reaches the northern convection region, completing a full cycle. The oscillation timescale here is determined by the time consumed in transporting the Southern Ocean salinity anomaly to the North Atlantic. A shortcoming of this study is that their analysis was largely based on zonal mean Hovmöller diagrams, potentially omitting certain important information (e.g., the spatial structure). Although sharing the similar origin (the Southern Ocean) and timescale to that of Park and Latif (2008), it is likely that these two studies correspond to different modes of the AMOC because of their significant difference in dominating process. Perhaps an inter-hemispheric theoretical model like the one used in Scott et al. (1999) can provide an explanation for the mechanism of Delworth and Zeng (2012), while no direct linkage between any theoretical model and their modeling study has been proposed.

Recently, a group of studies stressed the role of the Arctic Ocean in the AMOC MCO. Jiang et al. (2021) identified a 200-year AMOC oscillation in their IPSL-CM6-LR model simulation. When the AMOC resides in its strong phase, the Arctic Ocean is warmed and thus more sea ice melting and southward freshwater transport will hamper the subpolar deep convection and drive the AMOC into its negative phase. This is the “Arctic Ocean origin” paradigm, reflecting another multicentennial AMOC mode dominated by the Arctic Ocean. Meccia et al. (2022) found a 150-year AMOC oscillation in the EC-Earth3 model with a similar mechanism. Similarity in explanations proposed by these two studies is possibly because both models use the same ocean component (NEMO 3.6). However, whether their timescales could actually be considered as multicentennial remains debatable. The mean strengths of the AMOC at 30°N in Jiang et al. (2021) and Meccia et al. (2022) are 10.8 and 16.3 Sv, respectively, corresponding to the oscillation periods of 200 and 150 years, respectively. It is conceivable that under the realistic AMOC strength of 17-18 Sv (McCarthy et al. 2015; McCarthy et al. 2020), the AMOC oscillation periods of these two studies might be shortened to centennial timescale. There is indeed a longer (270 years) oscillation found by Mehling et al. (2022) with a mechanism similar to the “Arctic Ocean origin” paradigm, while the model they used is of intermediate complexity.

So far, the dominating processes emphasized in existing coupled model studies are highly diverse. Although it is possible that they can correspond to different multicentennial modes of the AMOC in reality, they do not have robust support from theoretical studies. It is thus possible that the multicentennial modes found in modeling results cannot capture the essence of the AMOC MCO if there is no theoretical support. Similarly, a theory alone is not convincing enough if it cannot be verified by modeling studies. Our previous theoretical studies encouraged us to conduct a necessary coupled model study, in order to validate both theoretical and coupled model results. If the results of a coupled model with the highest complexity can be explained by a theoretical model with the lowest complexity, this may improve the credibility of the “North Atlantic origin” eigenmode we proposed and advance our understanding of the AMOC MCO.

By analyzing the results from a coupled model control simulation, we identify an MCO of the AMOC with dominating processes mainly in the North Atlantic. The dynamic mechanism of the modeled MCO can be explained by the theory proposed in LY22. We organize this paper as follows.

In section 2, we describe the model, the experiment, and the approach for extracting low-frequency variability from the raw data. In section 3, we show the MCOs of the AMOC and global buoyancy fields. The relative contributions to sea-surface density (SSD) from sea-surface temperature (SST) and salinity (SSS) are then analyzed. In section 4, detailed processes leading to the AMOC MCO are revealed, and the spatial structures related to this oscillation are illustrated. In section 5, we provide a dynamic explanation for this mode. Section 6 presents the summary and discussion.

2. Model and methods

a. Pre-industrial control simulation

The coupled model employed is the Community Earth System Model (CESM, version 1.0.4) developed by the National Centre for Atmospheric Research (NCAR). It is a global climate model consisting of five components: atmosphere, land surface, ocean, sea ice, and ice sheet. A coupler exchanges data between these components.

The model grid we use is f19_gx1v6. The atmospheric component is the Community Atmosphere Model version 4 (CAM4) (Neale et al. 2010), with 26 vertical levels and a horizontal resolution of 1.9°×2.5°. The land surface model is the Community Land Model version 4 (CLM4) (Lawrence et al. 2011), with the same horizontal resolution as CAM4. The ocean model is the Parallel Ocean Program version 2 (POP2) (Smith and Gent 2010). It uses the gx1v6 curvilinear grid, having 384×320 grid points horizontally and 60 layers vertically. The horizontal grid is zonally uniform at a 1.125° resolution but meridionally non-uniform, with a 0.27° resolution near the equator, increasing to 0.65° at 60°N/S and then decreasing toward the polar regions. The sea ice model is the Community Ice Code (CICE4) (Hunke and Lipscomb 2010), with the same horizontal resolution as POP2. The coupler is the CESM Coupler CPL7 (Craig et al. 2012).

In the ocean model, velocity is divided into three components: explicit Eulerian-mean velocity, parameterized bolus velocity, and parameterized sub-mesoscale velocity (Gent and Mcwilliams 1990; Fox-Kemper and Ferrari 2008; Fox-Kemper et al. 2008); the latter two are collectively regarded as the parameterized eddy-induced velocity. These three velocity components have their corresponding transport or streamfunction. The total, or referred to as “residual,” velocity (streamfunction) is the sum of these three components. We conduct a 2500-year control simulation from the rest with pre-industrial configuration, to assure that the thermohaline circulation has reached its equilibrium before our study period. In this study, we analyze outputs of the last 1500 years.

b. Data analysis methods

Instead of using the traditional empirical orthogonal function (EOF) method, we adopt the low-frequency component analysis (LFCA) method (Wills et al. 2018) to evaluate the low-frequency AMOC variability. The LFCA provides linear combinations of the first n EOFs and principal components (PCs) of the data. The results are n low-frequency patterns (LFPs) as the spatial patterns and n corresponding low-frequency components (LFCs) as the time series. The LFPs and corresponding LFCs are ranked in a descending order according to the ratio of their low-frequency variances (obtained through a low-pass filter) to the total variance of the first n EOFs. Therefore, low-frequency signals are the most concentrated in LFP1 and LFC1, which are our focus. Please refer to Wills et al. (2018) for more detailed introduction to the LFCA method, and for the evaluation on the relative advantages of using EOF or LFCA.

As demonstrated in Jiang et al. (2021), the LFCA outperforms the EOF method in extracting and analyzing low-frequency variability of the AMOC. A Lanczos filter with 121 weights and 60 years cut-off period is used for the LFCA and for filtering other time series throughout the paper. Power spectral analysis is conducted for both the unfiltered AMOC index and AMOC LFC1. Significance at 95% confidence level and the best-fit first-order Markov red noise spectrum are presented along with the power spectrum.

3. MCOs in the coupled model

a. AMOC

We find a clear MCO in the time series of the AMOC index (Fig. 1a), with the most significant peak around 375 years (Fig. 1b). The AMOC index is defined as the maximum total meridional streamfunction within the North Atlantic region spanning 20°-70°N and 200-3000 m. The time series of the AMOC index shows a stable oscillation around one equilibrium, with the magnitude around ± 2 Sv, about 10% of the climatological value (24 Sv). The climatological AMOC exhibits an overall northward branch in the upper 0-1000 m, a deep convection branch around 60°N, and a southward NADW branch in the deep ocean of 1500-3000 m (Fig. 1e). The maximum value is located near 1000 m at around 40°N.

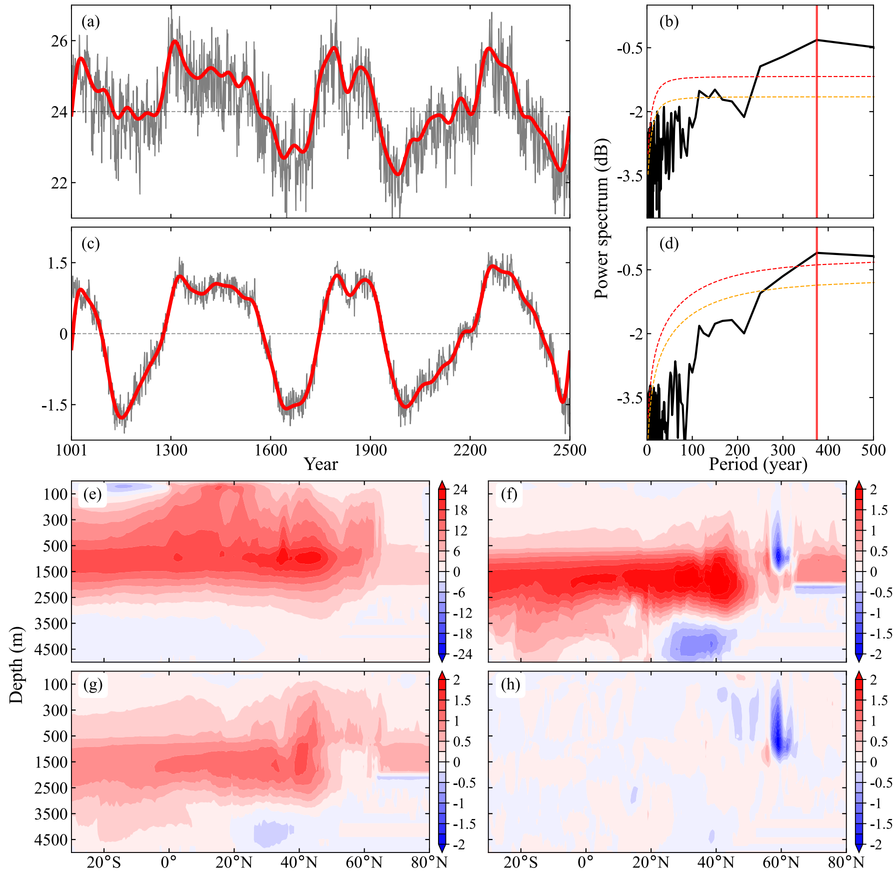

FIG. 1. (a) Time series for the AMOC index (units: Sv; 1 Sv = 10^6 m^3 s^{-1}) of model years 1001-2500. The AMOC index is defined as the maximum total meridional streamfunction in the North Atlantic spanning 20°-70°N and 200-3000 m. The gray curve represents the unfiltered AMOC index, and the red curve is the low-pass-filtered AMOC index using the Lanczos filter. The horizontal dashed line denotes the climatological value of the AMOC (24 Sv). (b) Power spectrum (units: dB) of the unfiltered AMOC index, with period as the abscissa. The dashed red and orange curves represent the best-fit first-order Markov red noise spectrum and its significance at 95% confidence level, respectively. The vertical red line denotes the most significant peak (375 years). (c) Same as (a), but for the AMOC LFC1. Before applying the LFCA method, the data is detrended and then weighted according to the square root of grid cell thicknesses. The Lanczos filter is used for the LFCA. (d) Same as (b), but for the AMOC LFC1. (e) Climatological pattern of the total AMOC averaged over years 1001-2500 (units: Sv). (f) Pattern of the AMOC LFP1 (units: Sv). (g) and (h) are the regression patterns of the Eulerian-mean and eddy-induced AMOCs on the AMOC LFC1 (units: Sv), respectively.

To better depict the low-frequency variability of the AMOC, we apply the LFCA method to the total AMOC. The first 10 EOFs are utilized, which explain 93.7% of the total variance. High-frequency signals of the AMOC are substantially weakened in the AMOC LFC1 (Fig. 1c). Power spectrum of the AMOC LFC1 shows that the most significant peak persists near 375 years and becomes the only peak passing the significance test (Fig. 1d). The variance of the AMOC LFP1 accounts for 87.5% of the low-frequency variance of the first 10 EOFs. The pattern of the AMOC LFP1 (Fig. 1f) aligns with that of the climatological AMOC (Fig. 1e), but exhibits a structure with negligible transport above 500 m. The upper ocean wind-driven subtropical cell, which is discernible in the climatological AMOC pattern (Fig. 1e), has been filtered out in the AMOC LFP1 (Fig. 1f). This suggests that the multicentennial variability of the AMOC may primarily occur in the lower ocean, and the high-frequency variability that may be related to the upper ocean wind-driven circulation should be ruled out.

The Eulerian-mean component of the AMOC demonstrates a coherent meridional variability throughout the Atlantic basin (Fig. 1g), while its eddy-induced component has a significant local variability within the subpolar North Atlantic (Fig. 1h). It is noteworthy that the fluctuation of the eddy-induced AMOC is of comparable magnitude to that of the Eulerian-mean AMOC, but with an opposite sign in the subpolar deep convection region, resulting in the negative signal at the same position of the AMOC LFP1 (Fig. 1f). This suggests that a stronger (weaker) Eulerian-mean AMOC is associated with a weaker (stronger) eddy-induced AMOC. This was deliberated in LY22. Although the causality between the Eulerian-mean and eddy-induced AMOCs is not yet clear, Figs. 1f and 1h suggest that the eddy-induced AMOC plays a role in the AMOC MCO.

b. Global SSD, SSS, and SST

Consistent with the AMOC LFC1, the surface buoyancy fields of the global ocean also exhibit remarkable MCOs (Fig. 2). We conduct the LFCA on the global SSD anomaly, SSD anomaly induced by SSS anomaly, and SSD anomaly induced by SST anomaly according to Roquet et al. (2015). Their LFC1s all reflect multicentennial variability (Fig. 2a). Moreover, the SSD anomaly is mainly caused by the SSS anomaly (Fig. 2a, black and red curves), while is offset slightly by the SST anomaly (Fig. 2a, blue curve).

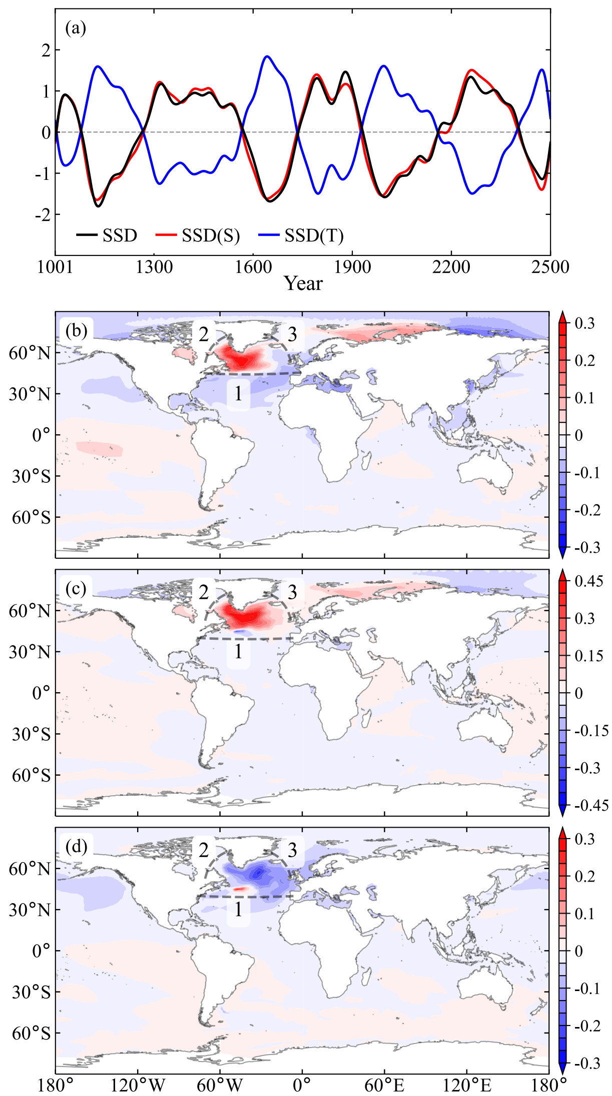

FIG. 2. (a) Filtered LFC1s (units: dimensionless) of the global SSD anomaly (black curve), SSD anomaly induced by SSS anomaly (red curve), and SSD anomaly induced by SST anomaly (blue curve). (b) LFP1 (units: kg m^{-3}) of the global SSD anomaly. (c) and (d) are the same as (b), but for the SSD anomalies induced by SSS and SST anomalies, respectively. Before the LFCA, the data is detrended and then weighted according to the square root of grid cell areas. The Lanczos filter is applied in (a); and the LFCA, in (b)-(d). The “encircled region” enclosed by dashed curves in Figs. 2b-d will be used in Fig. 11 for calculation. These dashed curves are parallel to the grid lines of the ocean model. Dashed curve 1 is along 45°N.

The LFP1s of the global buoyancy fields indicate that the strongest multicentennial signals are located in the North Atlantic (Figs. 2b-d), particularly in the NADW formation region of the subpolar North Atlantic with the deepest March mixed layer depth simulated (figure not shown). The spatial patterns in Figs. 2b-d are nearly identical, further indicating that in both the North Atlantic and Arctic Ocean, the SSD anomalies (Fig. 2b) are dominated by the SSS anomalies (Fig. 2c), while partly canceled by the SST anomalies (Fig. 2d). Note the presence of the so-called “transition zone” near

40°N along the Gulf Stream extension (Buckley and Marshall 2016). The local density variability in the transition zone is negligible (Fig. 2b) due to the counteractive effects from anomalous salinity and temperature. Multicentennial signals in the other basins, such as the South Atlantic, Southern Ocean, and the Pacific and Indian Oceans, are rather weak. Figure 2 suggests that the North Atlantic acts as a pacemaker for the multicentennial variability of the Earth's climate system, which can be attributed to the AMOC.

4. Evolution of salinity anomalies in the Atlantic

a. Latitude-depth patterns

Let us first examine the model distribution of climatological salinity in the Atlantic (Fig. 3). In the North Atlantic, the meridional gradient of climatological salinity is generally greater in the upper ocean and decreases with depth. Specifically, the most saline water (salinity higher than 36.5 psu) is located in the subtropical upper ocean between 20°N and 40°N, extending downward to 1500 m and then southward to 40°S in the deep ocean. The more saline subtropical water is separated from the fresher subpolar water by the Gulf Stream extension and the North Atlantic Current (NAC), forming the subpolar front near 45°N, whose location is consistent with the downward branch of the AMOC (Fig. 1e). The more saline subtropical water can also extend northward to the subpolar subsurface ocean, against the freshwater from the Arctic. On the other hand, fresher water (salinity lower than 34 psu) comes mainly from the surface of the subpolar Southern Ocean, extending downward and northward and occupying the southern subtropical ocean between 200 and 1500 m, known as the Antarctic intermediate water.

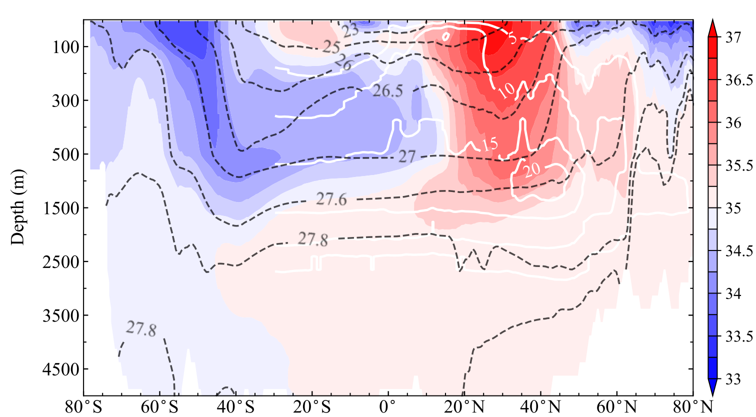

FIG. 3. Climatological salinity zonally averaged in the Atlantic (shading; units: psu), superimposed with climatological potential density (σ_θ) (dashed black contour; units: kg m^{-3}) and AMOC (white contour; units: Sv).

Next, we investigate how the salinity anomalies evolve with the AMOC at the multicentennial timescale. Figure 4 illustrates the lead/lag regression coefficients of the zonally averaged salinity anomalies in the Atlantic on the AMOC LFC1, superimposed with climatological potential density (σ_θ). When the salinity anomalies lead the AMOC LFC1 by 200 years (Fig. 4a), there is a pronounced negative salinity anomaly centered in the upper ocean around 55°N, corresponding to the weakest NADW formation and AMOC. This negative salinity anomaly extends from the surface to deep ocean of the North Atlantic north of 45°N, and occupies 1500-3500 m in the deep ocean south of 45°N. South of the subpolar negative salinity anomalies, broad positive salinity anomalies are observed at lower latitudes, occupying the upper 1500 m of the Atlantic. The negative salinity anomalies are the strongest in the subpolar upper ocean, while the positive salinity anomalies have the greatest magnitude in the subtropical intermediate ocean between 500 and 1500 m. This dipole structure is the most robust feature throughout the entire evolution of salinity anomalies in the North Atlantic.

The evolution of salinity anomalies at the multicentennial timescale is closely linked to the evolution of the AMOC. The downward and southward movements of salinity anomalies north of 45°N correspond to a strong convection or vertical mixing, and the mean advection by the lower branch of the AMOC, respectively. The northward and upward movements of salinity anomalies south of 45°N go roughly within 26.5-27.6 σ_θ, corresponding to the mean advection by the upper branch of the AMOC. These two salinity anomalies circulate in the North Atlantic, changing their phases during their movements (Fig. 4). The salinity anomalies in the South Atlantic are weak, having negligible contributions to salinity variation in the North Atlantic.

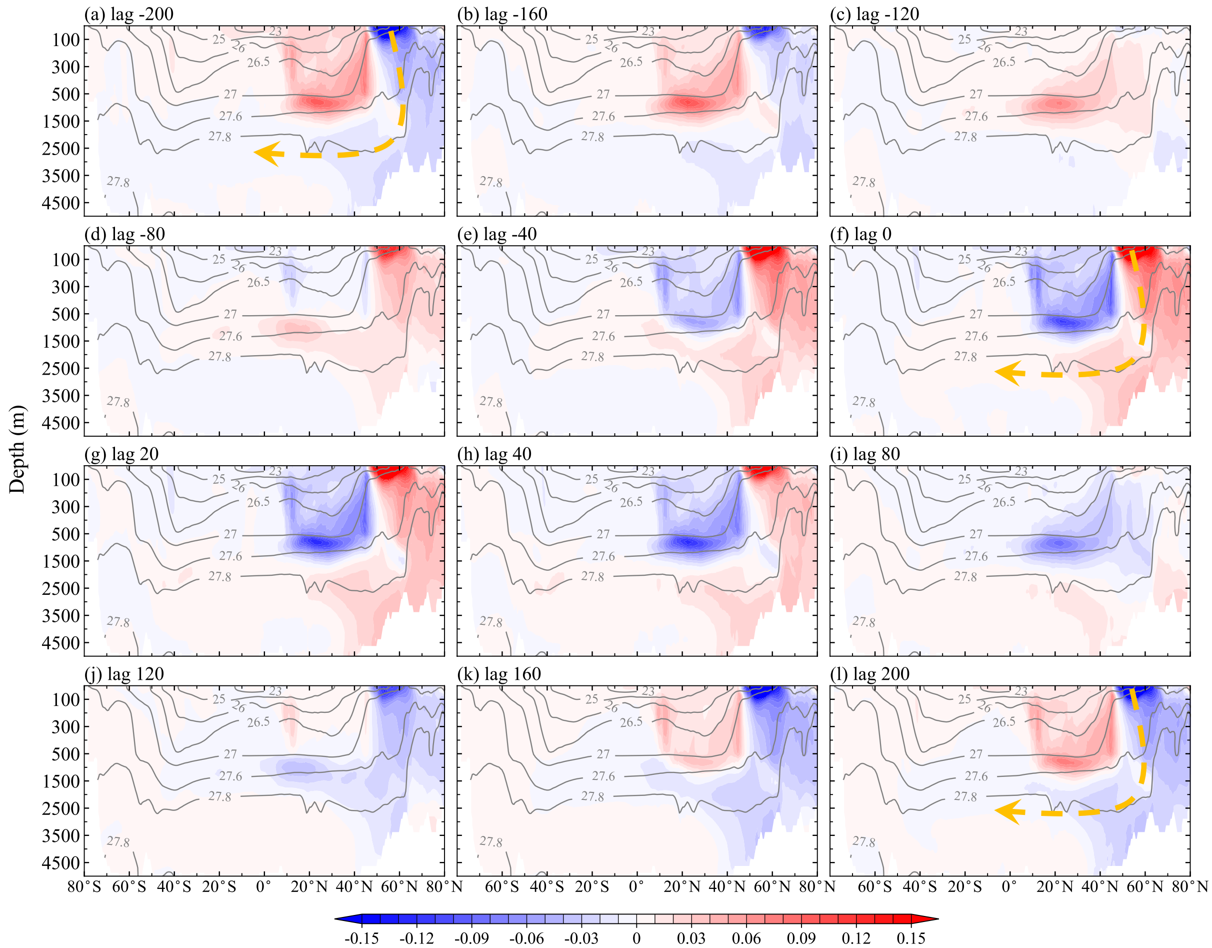

FIG. 4. Lead/lag regression coefficients of zonally averaged salinity anomalies in the Atlantic on the AMOC LFC1 (shading; units: psu). Negative lag means the AMOC LFC1 lags the salinity anomalies (units: year). Contours show the zonally averaged climatological potential density σ_θ in the Atlantic (units: kg m^{-3}). Dashed orange arrows in (a), (f), and (l) show schematically the downward and southward movements of salinity anomalies.

Specifically, during the period when the salinity anomalies lead the AMOC by 200-120 years (Figs. 4a-c), the salinity anomalies north of 45°N are negative and the AMOC is in a weak regime. The magnitude of negative anomalies decreases with time, indicating an on-going phase transition from a weak to a strong AMOC regime. The positive salinity anomaly in the subtropical intermediate ocean moves northward from ~40°N and upward along 26.5-27.6 σ_θ (Fig. 4c), helping neutralize the negative salinity anomaly in the NADW formation region and furthering its phase shift to positive (Fig. 4d). When the salinity anomalies lead the AMOC by 80-0 years, the positive salinity anomalies north of 45°N develop gradually (Figs. 4d-f) and eventually reach the maximum magnitude at lag 0 years (Fig. 4f), which also mirrors the similar evolution of the AMOC. The subpolar upper salinity anomaly is transported downward through convection or vertical mixing, then propagates southward in the deep ocean (Fig. 4, orange arrows). Meanwhile, negative salinity anomalies grow in lower latitudes near 26.5-27.6 σ_θ. Afterward, the AMOC starts to decrease and the evolution of salinity anomalies enters the opposite phase (Figs. 4g-l). Throughout the entire cycle, salinity anomalies in the Arctic region and Atlantic deep ocean are largely synchronized with and influenced by the subpolar upper ocean. Salinity anomalies in the South Atlantic are weak and have nearly no impact on the North Atlantic.

Overall, the major evolution characteristics of salinity anomalies in the North Atlantic are reflected in three levels: (i) the upper ocean around 0-200 m, where the subpolar salinity anomaly is the strongest and develops locally, (ii) the intermediate ocean around 26.5-27.6 σ_θ, where the salinity anomalies south of 45°N evolve, and propagate northward to weaken the subpolar upper salinity anomaly, and (iii) the deep ocean around 27.8 σ_θ, where the salinity anomalies originate from the subpolar upper ocean and propagate southward.

Figure 5 clearly shows the local development of salinity anomaly in the subpolar upper ocean and the northward (southward) propagation of salinity anomalies in the intermediate (deep) ocean. Based on Fig. 4, we vertically average the salinity anomalies over these three levels and then calculate their lead/lag regression coefficients on the AMOC LFC1. In the upper ocean (Fig. 5a), the most remarkable signal is located in 45°-65°N, which shows a local periodic oscillation without robust connection with signals in both the subtropical and polar regions. In the 26.5-27.6 σ_θ intermediate ocean (Fig. 5b), salinity anomaly at 45°N shows a northward propagation (white arrows), suggesting its influence on the subpolar region. Salinity anomaly near 20°N appears to develop locally with the opposite sign to that north of 45°N. In the 27.75-27.85 σ_θ deep ocean (Fig. 5c), salinity anomalies propagate southward from the subpolar to equatorial and South Atlantic (white arrows). In all three levels, the maximum regression coefficient at the subpolar region occurs when the salinity anomalies lead the AMOC LFC1 by around 10 years (Fig. 5, orange dot).

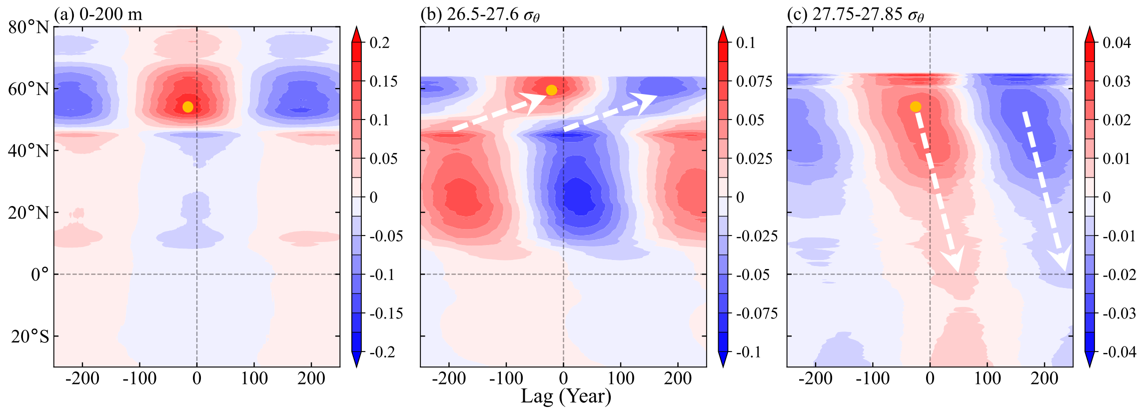

FIG. 5. Lead/lag regression coefficients of zonally and vertically averaged salinity anomalies in the Atlantic on the AMOC LFC1 (units: psu). (a) Averaged over 0-200 m, (b) averaged over 26.5-27.6 σ_θ, and (c) averaged over 27.75-27.85 σ_θ. The orange dot denotes the position of the maximum regression coefficient. In (b) and (c), salinity anomalies shallower than 200 m or north of 65°N are removed. The dashed white arrows show schematically the meridional propagations of salinity anomalies in the intermediate-deep oceans. Note that the colorbars for the three subplots are different. Negative lag means the AMOC LFC1 lags the salinity anomalies (units: year).

b. Horizontal patterns

To explain the evolutions of salinity anomalies in these three levels and depict their horizontal patterns, we plot their horizontal lead/lag regression maps of salinity anomalies on the AMOC LFC1 in Figs. 6, 8, and 10, superimposed with climatological currents. In the North Atlantic upper ocean, the climatological currents are featured with the northward Gulf Stream and its eastward extension, the northeastward NAC, and the subpolar cyclonic circulation occupying the Labrador Sea, eastern Greenland Sea and Irminger Sea (Fig. 6). Under this background mean circulation, the direct meridional exchange of salinity anomalies across 45°N is not easy, due to the blocking of the "transition zone" and NAC in the central and eastern Atlantic near 45°N. The salinity anomaly in the subpolar upper ocean evolves mostly locally without clear influence from the mean advection. For example, when the subpolar salinity anomaly changes from negative to positive (Figs. 6a-f), the subtropical salinity anomaly is always out of phase with it, no continuous propagation of salinity anomaly through the mean circulation is reflected. Similarly, when the subpolar salinity anomaly changes from positive to negative (Figs. 6g-l), there is also no contribution from the mean advection of the subtropical salinity anomaly. During the period of neutral salinity anomaly in the subpolar upper ocean (Figs. 6c, i), there appears to be weak salinity anomaly in the subtropical upper ocean that can be advected eastward by the NAC, and then northwestward to invade the subpolar basin by the Irminger current. However, this mean advection of salinity anomaly is too weak and may not be enough to support the phase transition of the subpolar salinity anomaly in Figs. 6c and 6i. In general, mean advection of salinity anomaly in the North Atlantic upper ocean does not work for the AMOC MCO.

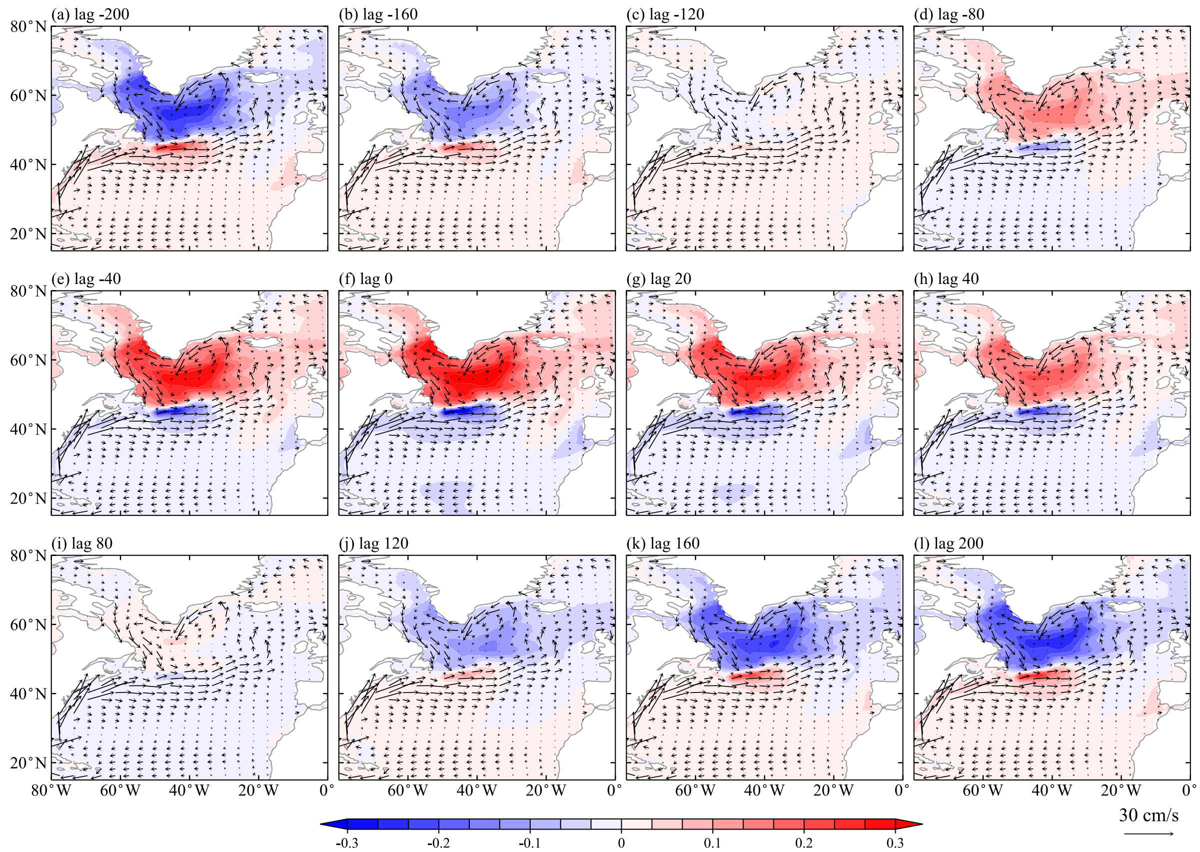

FIG. 6. Lead/lag regression coefficients of salinity anomalies averaged over 0-200 m on the AMOC LFC1 (units: psu), superimposed with climatological currents averaged over the same depth range (vector; units: cm s^{-1}). Negative lag means the AMOC LFC1 lags the salinity anomalies (units: year).

The perturbation advection of mean salinity in the North Atlantic can well explain the evolution of salinity anomaly in the subpolar upper ocean (Fig. 7). Figure 7 shows the lead/lag regression coefficients of current anomalies vertically averaged over 0-200 m on the AMOC LFC1, overlaid with climatological salinity. During the enhancing period of the subpolar positive salinity anomaly (Figs. 6d-f), the eastward and northward NAC is also enhancing (Figs. 7d-f), which can effectively transport more saline water from the mid-latitude eastern Atlantic to the subpolar Atlantic and enhance the subpolar positive salinity anomaly. Similarly, during the enhancing period of the subpolar negative salinity anomaly (Figs. 6j-l), the eastward and northward NAC is weakening (Figs. 7j-l), which reduces the northward transport of saline water from the mid-latitude eastern Atlantic and enhances the subpolar negative salinity anomaly. Therefore, the salinity anomaly in the subpolar upper ocean and thus the AMOC anomaly are always enhanced by the perturbation advection. This is the well-known positive feedback between the subpolar salinity anomaly and the perturbation circulation (Stommel 1961; Nakamura et al. 1994; Marotzke and Stone 1995; Sévellec et al. 2006).

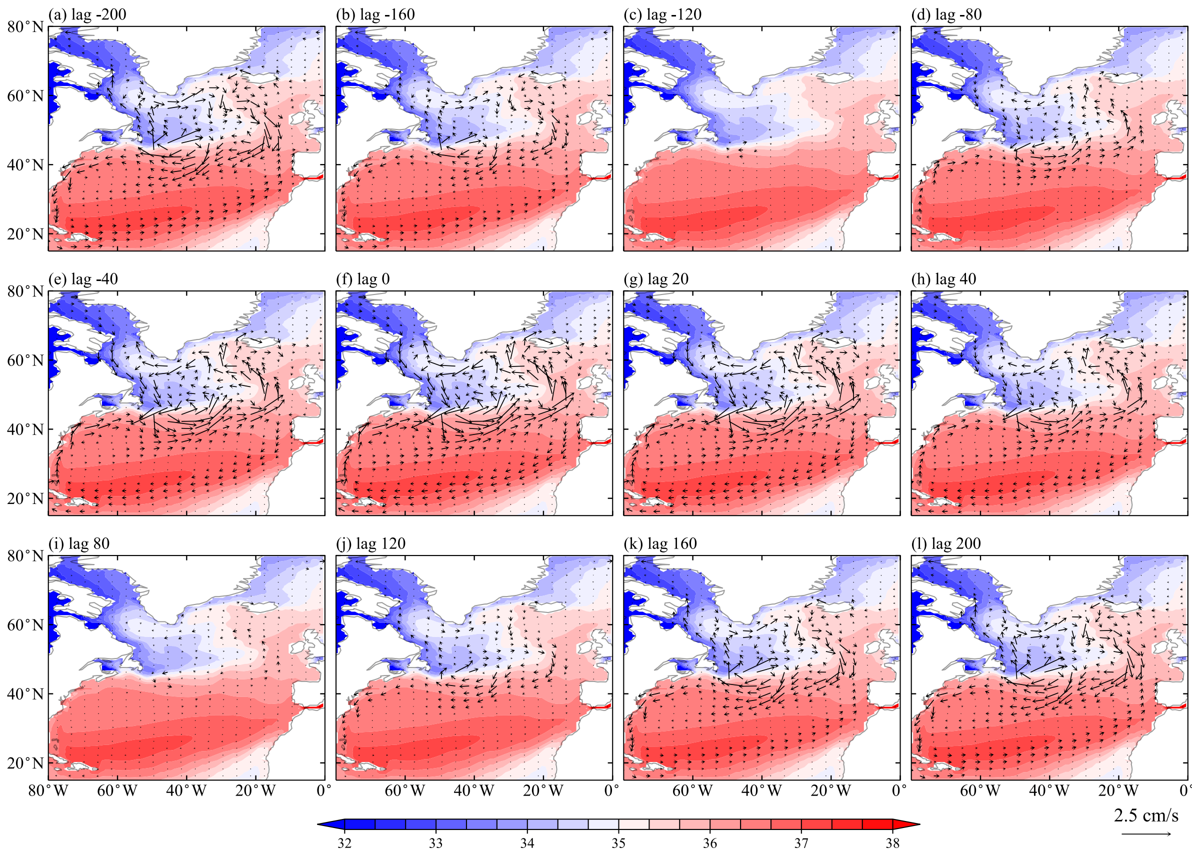

FIG. 7. Lead/lag regression coefficients of current anomalies averaged over 0-200 m on the AMOC LFC1 (units: cm s^{-1}), superimposed with climatological salinity averaged over the same depth range (shading; units: psu). Negative lag means the AMOC LFC1 lags the current anomalies (units: year).

It is the mean advection of salinity anomaly in the intermediate ocean that weakens the subpolar upper salinity anomaly. In the intermediate North Atlantic (Fig. 8), there exhibits clear advection of salinity anomalies from the mid-latitude eastern Atlantic to the subpolar basin. To include the propagation of salinity anomalies in the lower latitudes, Fig. 8 spans the latitudes from 30°S to 80°N. The salinity anomalies shallower than 200 m are removed, resulting in white area in most of the subpolar basin (Fig. 8), where the climatological density exceeds 27.6 σ_θ. Influence of the mean advection of subtropical salinity anomaly on the eastern subpolar basin is greater in the intermediate ocean than in the upper ocean. Particularly, when the subpolar upper salinity anomaly changes from negative to positive (Figs. 6a-f), the subtropical salinity anomaly with the opposite sign can be advected eastward, northward, and upward by the mean NAC along isopycnals (Figs. 8a-f), reducing the subpolar upper salinity anomaly and contributing to its phase change. Similar situation also occurs when the subpolar upper salinity anomaly changes from negative to positive (Figs. 6g-l, 8g-l). This is the negative feedback between the subpolar upper salinity anomaly and the mean advection. When this negative feedback exceeds the positive feedback between the subpolar upper salinity anomaly and the perturbation advection seen in Fig. 7, the magnitude of subpolar upper salinity anomaly reaches the maximum and starts to decrease (Figs. 6a, f, l), which facilitates the sustained AMOC MCO.

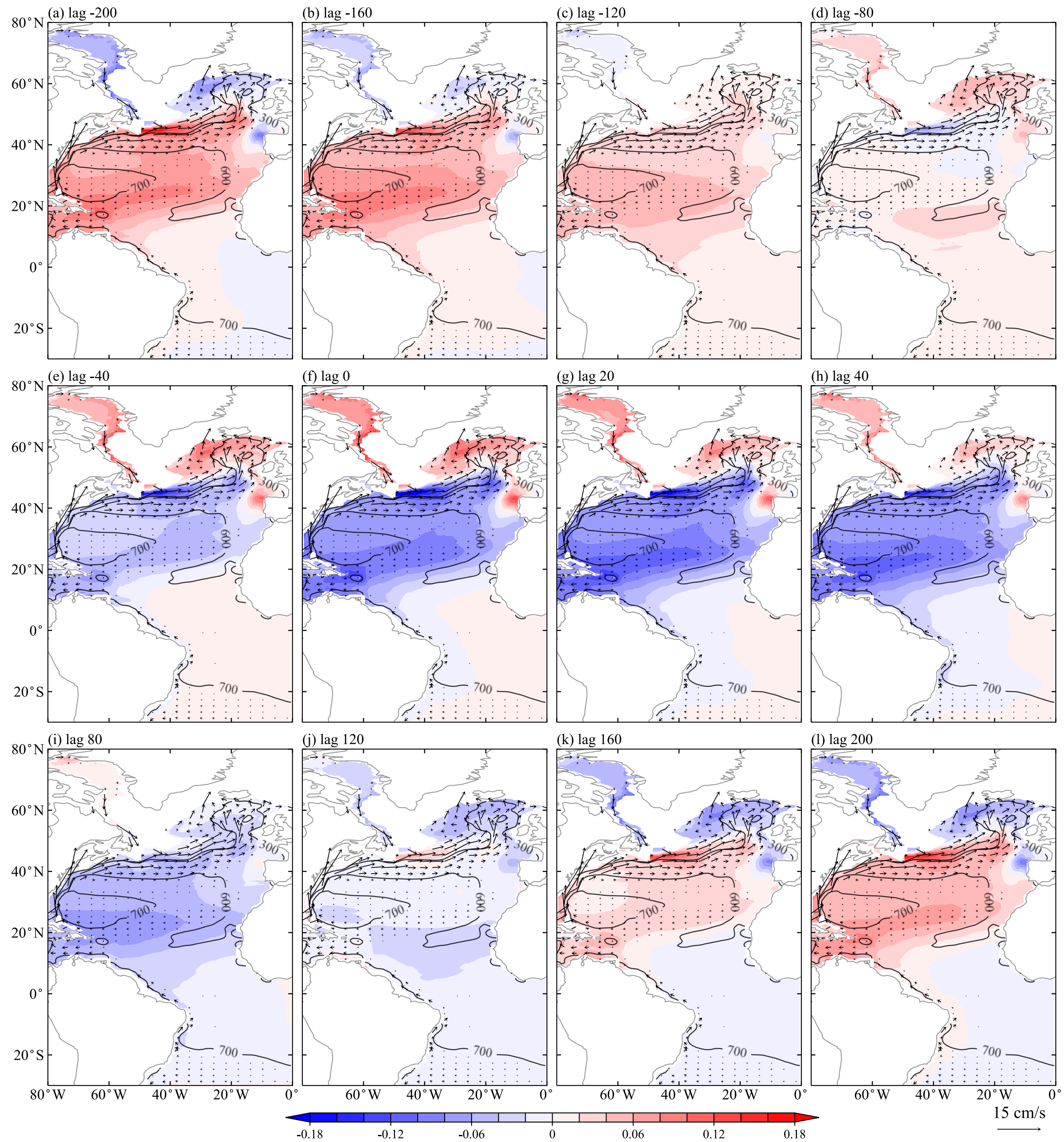

FIG. 8. Same as Fig. 6, but for variables averaged over 26.5-27.6 σ_θ. Black contours represent mean depths of 26.5-27.6 σ_θ (units: m). Currents weaker than 0.4 cm s^{-1} are not plotted. The 0-200 m salinity and current anomalies are removed to exclude the influence from the upper ocean, resulting in the blank regions in the subpolar basin.

Both Figs. 8 and 5b show clear salinity anomalies in the subtropics, which are always out of phase with those in the subpolar ocean. These salinity anomalies reflect a weak propagation along the low-latitude western boundary, against the mean western boundary current (Fig. 8). The growth of these salinity anomalies is through the perturbation circulation. Figure 9 presents the lead/lag regression coefficients of current anomalies averaged over 26.5-27.6 σ_θ on the AMOC LFC1, overlaid with climatological salinity. In the intermediate Atlantic of 0°-30°N (Fig. 9), the climatological salinity is the highest in the northeast, decreasing southwestward to 20°N and further decreasing southward along the western boundary. The perturbation circulation occurs primarily along the gradient of the climatological salinity and western boundary, leading to the salinity anomalies aligned with this trajectory (Fig. 8). For example, when the tropical circulations are weakening (Figs. 9a-c), the subtropical positive salinity anomalies also weaken (Figs. 8b-d), because of the weakened southwestward transport of salinity anomalies through the perturbation circulation at 20°-30°N. Similarly, when the tropical circulations are enhancing (Figs. 9d-f), the subtropical negative salinity anomalies also enhance (Figs. 8e-g), because of the increased perturbation advection of freshwater from the lower latitudes. The majority of the subtropical salinity anomalies circulates within the subtropical anticyclonic gyre, and can be collectively considered as an antiphase signal to the salinity anomaly in the subpolar upper ocean.

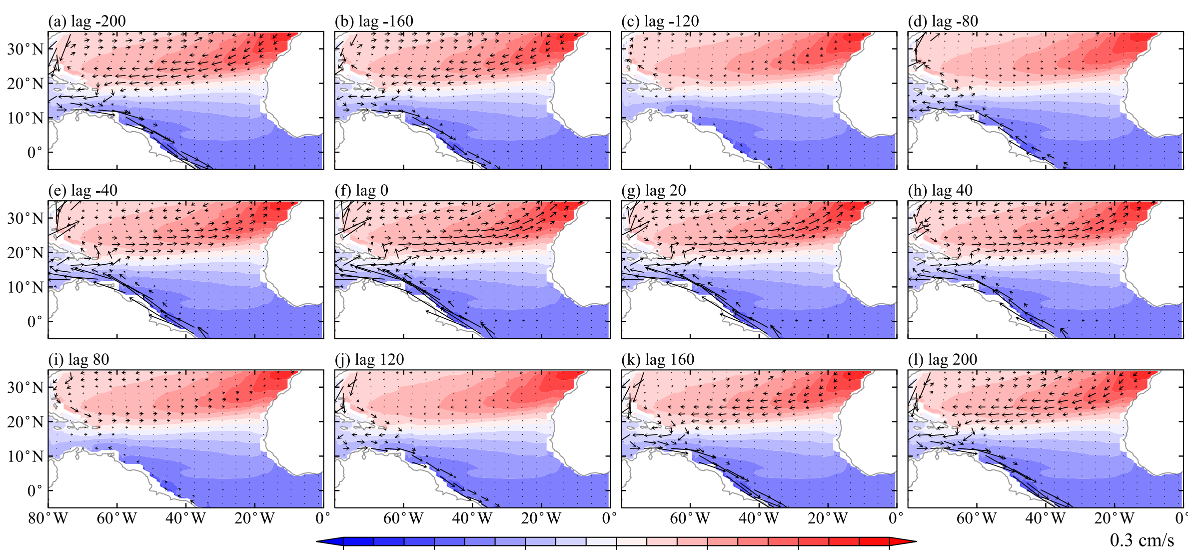

FIG. 9. Same as Fig. 7, but for variables averaged over 26.5-27.6 σ_θ and spanning 5°S-35°N, to highlight circulation anomalies in the tropics.

In summary, the mean advection of salinity anomaly in the intermediate ocean plays a critical role in the evolution of the subpolar upper salinity anomaly. There is a clear connection between the subtropical and subpolar salinity anomalies, consistent with that observed in Fig. 5b. The mean advection of the subtropical salinity anomaly into the subpolar region weakens the subpolar upper salinity anomaly, balancing the perturbation advection in the upper ocean and leading to the phase change of the AMOC. Salinity anomalies in the subtropical basin are dominated by the perturbation circulation in the tropical regions. Again, at the multicentennial timescale, the salinity anomalies in the South Atlantic are considerably weak.

In the deep ocean (Fig. 10), the evolution of salinity anomalies is dominated by mean advection. There is a coherent southward advection of salinity anomalies from the subpolar basin to the tropics through the mean southward currents, especially the deep western boundary current (DWBC). The deep ocean salinity anomalies have nearly the same polarity in the whole basin, and the same polarity as the salinity anomaly in the subpolar upper ocean, suggesting its positive effect on removing the subpolar upper salinity anomaly. The southward propagation can even cross the equator along the deep ocean western boundary, completing its movement in approximately 50 years, which can be estimated from Fig. 5c.

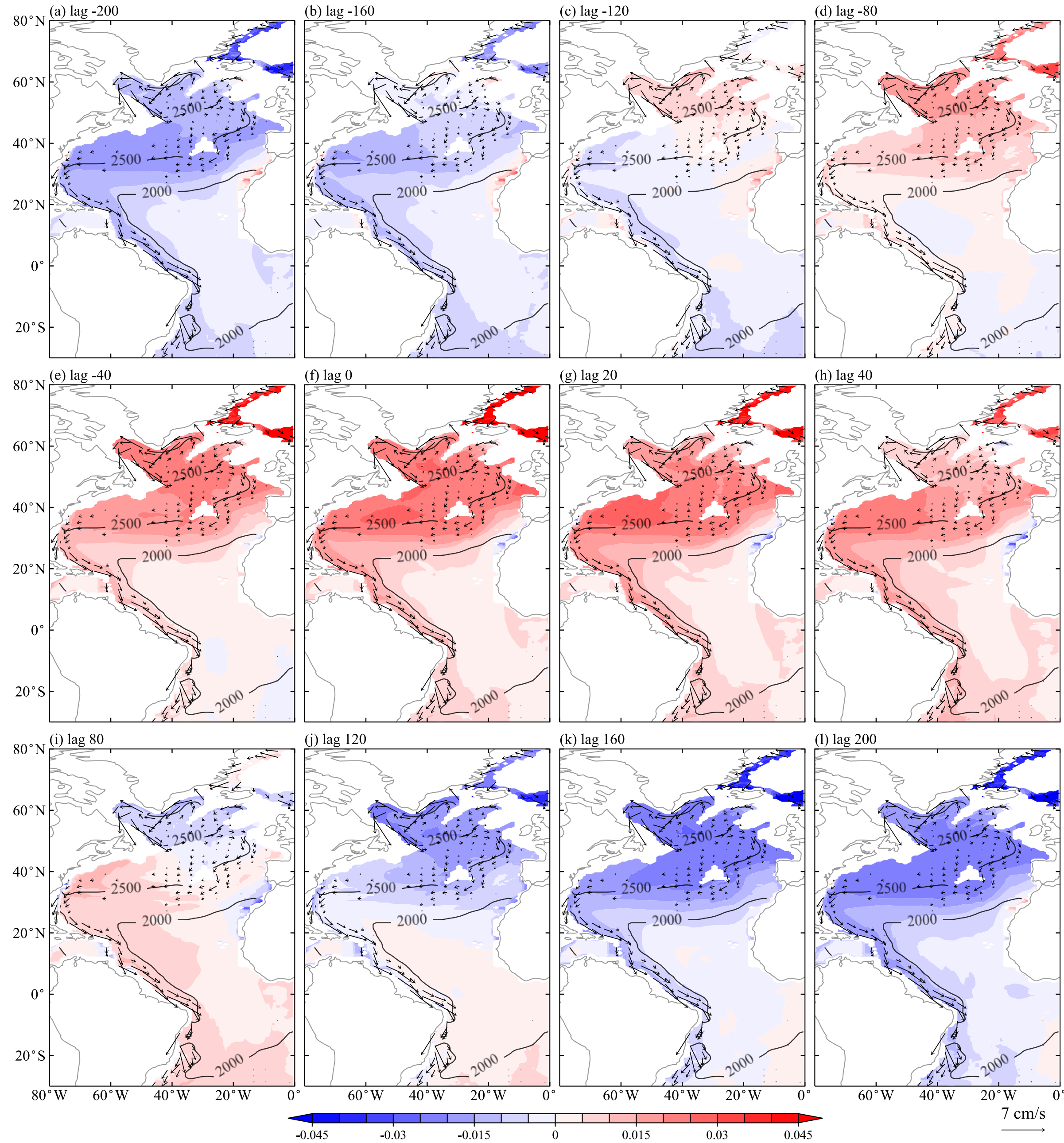

FIG. 10. Same as Fig. 8, but for variables averaged over 27.75-27.85 σ_θ. Black contours represent mean depths of 27.75-27.85 σ_θ (units: m). Currents weaker than 0.07 cm s^{-1} are not plotted. The 0-200 m salinity and current anomalies are removed to exclude the influence from the upper ocean, resulting in the blank regions in the subpolar basin.

c. Summary on collaborative changes in salinity and AMOC

Now, we have a clear 3-dimensional picture on how the salinity anomalies evolve in conjunction with the AMOC. Starting from the freshest subpolar upper ocean and thus the weakest AMOC (Fig. 6a), the mean NAC transports positive salinity anomalies northeastward and upward from the mid-latitude intermediate ocean to the subpolar region (Figs. 8a-c). This mean advection weakens the negative salinity anomaly in the subpolar upper ocean (Figs. 6a-c), leading to gradual recoveries of the AMOC and NAC (Figs. 7a-c), which in turn faciliates to neutralize the negative salinity anomaly itself. At the same time, the subpolar upper salinity anomaly is quickly transported downward to the deep ocean (Figs. 4a-c) and further advected southward by the mean DWBC (Figs. 10a-c). These processes take totally about 80-90 years, followed by the phase change of the subpolar salinity anomaly from negative to positive phase (Fig. 6d). Afterward, the positve salinity anomaly in the subpolar upper ocean increases the AMOC strength, which in turn leads to more northward saline water transport from the subtropical upper ocean (Figs. 7d-f). This reinforces the subpolar positive salinity anomaly (Figs. 6d-f) through the positive salinity advection feedback, and at the same time leads to negative salinity anomalies in the intermediate subtropics (Figs. 8e-g). The positve salinity anomaly in the subpolar upper ocean is transported downward (Figs. 4d-f) and then move southward (Figs. 10d-f) through the mean DWBC. These processes also take about 80-90 years. The evolution of salinity anomalies exhibits a dipole sturcture in the upper-intermediate oceans and a vertical baroclinic structure in the intermediate-deep oceans. Now, a half cycle of the evolutions of salinity anomalies and the AMOC is completed, which takes totally about 180 years; then, the evolutions enter the opposite phase.

5. Dynamics of the MCO

a. North Atlantic origin of the salinity anomalies

Salinity budget analysis reveals that the salinity anomaly in the subpolar North Atlantic mainly comes from the subtropics, while contributions from both the Arctic Ocean and the surface virtual salinity flux are minor (Fig. 11). Here, the salinity budget of the 0-1000 m subpolar upper ocean (the encircled region in Fig. 2) is analyzed, which is calculated as follows,

$$S_{net} = S_{LT}^1 + S_{LT}^2 + S_{LT}^3 + S_{bottom} \quad (1)$$

where S_{net} is the net salinity budget; S_{LT}^1, S_{LT}^2, and S_{LT}^3 are lateral transports of salinity from the subtropical basin, Labrador Sea and Arctic Ocean inward across the boundaries denoted by numbers 1, 2, and 3 in Fig. 2, respectively. S_{bottom} is the total salinity transport upward across the bottom of the encircled region at 1000 m. We also calculate the net surface virtual salinity flux (S_{VSF}) of the encircled region, including the local sea ice formation or melting, the net surface freshwater flux due to evaporation and precipitation, and river runoff. Furthermore, the lateral salinity transport S_{LT}^{i} can be decomposed into the transport due to the Eulerian-mean velocity (S_{Euler}^{i}) and those related to diffusion and eddy-induced velocity ($S_{Eddy+diff}^{i}$) as follows,

$$S_{LT}^{i} = S_{Euler}^{i} + S_{Eddy+diff}^{i}, \qquad i = 1, 2, 3 \tag{2}$$

In addition, we examine the Eulerian-mean velocity-induced salinity transports northward across boundary 1 (45°N) due to salinity anomaly $S_{S'\overline{V}}^{1}$ and velocity anomaly $S_{V'\overline{S}}^{1}$; that is, S_{Euler}^{1} is decomposed as follows,

$$S_{Euler}^{1} = S_{S'\overline{V}}^{1} + S_{V'\overline{S}}^{1} \tag{3}$$

Figure 11 shows that the lateral salinity transport northward across boundary 1 from the subtropical basin (S_{LT}^{1}) dominates the evolution of salinity anomaly in the subpolar upper ocean. The climatological transports or fluxes are removed. S_{LT}^{1} (Fig. 11a, solid black curve) is nearly seven times that of the transport from the north ($S_{LT}^{2} + S_{LT}^{3}$) (Fig. 11a, solid red curve). They all exhibit remarkable MCO, consistent with the LFC1s of the AMOC and global buoyancy fields (Fig. 2a). S_{LT}^{1} and $S_{LT}^{2} + S_{LT}^{3}$ are out of phase with each other, suggesting that when the salinity transport from the south is strong, the transport from the north is weak; and vice versa. Lead/lag regression analyses show that S_{LT}^{1} positively leads the AMOC LFC1 by about 20-30 years, while $S_{LT}^{2} + S_{LT}^{3}$ negatively lags the AMOC LFC1 by about 10 years, with the regression coefficient of the former also being seven times that of the latter (Fig. 11b). This confirms the dominant and driving role of salinity transport from the subtropical upper ocean in the AMOC variation, which in turn drives the variability in the Arctic Ocean. The bottom transport S_{bottom} is less than half of the magnitude of S_{LT}^{1} with the opposite phase (Figs. 11a, b, dashed black curves). Therefore, salinity transport from the bottom weakens the salinity anomaly in the subpolar upper ocean and facilitates its phase change.

The surface virtual salinity flux (S_{VSF}) (Fig. 11a, dashed red curve) is about two orders smaller than the lateral transports. S_{VSF} evolves nearly at the same pace as the lateral transports, but its magnitude is too small and thus its role in the AMOC variation can be neglected (Fig. 11b, dashed red curve). The contribution of S_{LT}^{1} is mainly from the Eulerian-mean transport S_{Euler}^{1} (Fig. 11c, black curve). The transport related to small-scale activities $S_{Eddy+diff}^{1}$ shows a similar oscillating behavior to S_{Euler}^{1} (Fig. 11c, red curve), while its magnitude is only one-seventh of the latter. Although near

45°N, the subpolar front tends to promote eddy activities and suppress the meridional velocity, S_{Euler}^{1} is still significantly greater than $S_{Eddy+diff}^{1}$. Furthermore, salinity transport variation due to the perturbation of Eulerian-mean velocity ($S_{V'\overline{S}}^{1}$) is much more important than that due to the salinity anomaly ($S_{S'\overline{V}}^{1}$) (Fig. 11e), driving the AMOC oscillation (Fig. 11f), and is consistent with Fig. 7.

In summary, the multicentennial salinity variation in the upper level of the subpolar North Atlantic is dominated by the perturbation of large-scale Eulerian-mean circulation in the subtropical-subpolar basin. Contribution from the Arctic Ocean is very weak. These results suggest that our "North Atlantic origin" paradigm is different from the previous "Arctic Ocean origin" and "Southern Ocean origin" paradigms, corresponding to a distinct North Atlantic-originated multicentennial mode of the AMOC. This mode has been predicted by the theoretical model in LY22. Next, we will examine the modeled mode using the theoretical model.

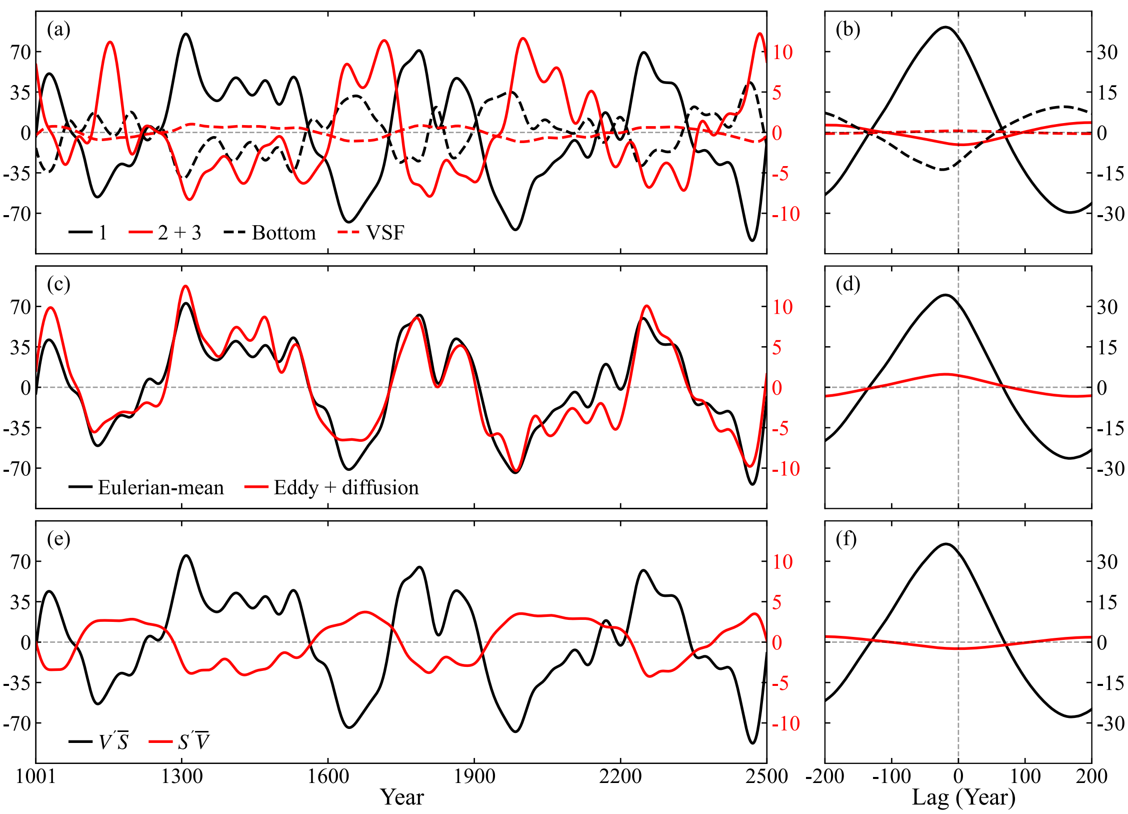

FIG. 11. Time series of salinity budget and the net surface virtual salinity flux of the 0-1000 m encircled region marked in Fig. 2, with their climatological values removed. (a) Total inward salinity transports across boundary 1 (solid black curve, left y-axis), boundaries 2+3 (solid red curve, right y-axis), bottom of the encircled region at 1000 m (dashed black curve, left y-axis), and the net surface virtual salinity flux (dashed red curve, right y-axis). (c) The lateral salinity transports induced by the Eulerian-mean velocity (black curve, left y-axis) and the sum of diffusion and eddy-induced velocity (red curve, right y-axis) northward across boundary 1. (e) Salinity transports due to the Eulerian-mean velocity anomaly ($V'\overline{S}$) (black curve, left y-axis) and salinity anomaly ($S'\overline{V}$) (red curve, right y-axis)

northward across boundary 1. (b), (d), and (f) show the lead/lag regression coefficients of terms in (a), (c), and (e) on the AMOC LFC1, respectively. Units for all curves are $Sv \cdot psu$. Negative lag means the AMOC LFC1 lags the salinity transports (units: year).

b. A theoretical explanation

The MCOs of the AMOC and salinity anomaly in the subpolar North Atlantic are mainly related to three dynamic processes: the perturbation advection of mean salinity (Fig. 7), the mean advection of salinity anomaly (Figs. 8, 10), and the convection or vertical mixing in the subpolar ocean (Fig. 4). The theoretical study in LY22 pinpointed that the salinity anomaly in the upper level of the subpolar North Atlantic is enhanced by the perturbation advection, while weakened by the mean advection and subpolar vertical mixing. Following the instruction of LY22 (appendix), we quantify these three processes in our coupled model next.

We divide the North Atlantic into four boxes (appendix) and focus on the salinity advection into the subpolar upper ocean and in the deeper ocean. For box 2, the mean advection, perturbation advection, and vertical mixing are represented by $\overline{q}(S_1' - S_2')$, $q'\left(\overline{S_1} - \overline{S_2}\right)$, and $-k_m(S_2' - S_3')$, respectively. Since the perturbation advection of mean salinity mainly occurs in the upper ocean, $\overline{S_1}$ and $\overline{S_2}$ are chosen to represent the subtropical and subpolar climatological salinities in Fig. 7, and thus given the values of 37 and 34.5 psu, respectively. S_1' and S_2' are anomalies of boxes 1 and 2, respectively. In the deeper ocean, $\overline{S_3}$ and $\overline{S_4}$ are the climatological salinities of boxes 3 and 4, respectively, and S_3' and S_4' are the corresponding anomalies. We set $\overline{q}$ to 15 Sv, which is smaller than the maximum meridional streamfunction in the North Atlantic (~24 Sv).

Figure 12 shows the MCOs of these dynamic processes similar to that of the AMOC. The enhancing effect of the perturbation advection and the weakening effects of the mean advection and vertical mixing in our coupled model results are well reflected, consistent with the theoretical study in LY22. Specifically, for the subpolar upper ocean, the perturbation advection $q'\left(\overline{S_1} - \overline{S_2}\right)$ (Fig. 12a, red curve) evolves at the same phase as the AMOC LFC1 (Fig. 12b, red curve). It always increases the amplitude of S_2' based on Eq. (A2), and eventually drives the AMOC oscillation. At the same time, the mean advection $\overline{q}(S_1' - S_2')$ (Fig. 12a, black curve) evolves at the opposite phase to the AMOC LFC1. It always weakens the amplitudes of S_2' and AMOC anomaly (Fig. 12b, black curve). The vertical mixing term $-k_m(S_2' - S_3')$ has roughly the same phase as the mean advection term, but with a much weaker amplitude (Figs. 12a, b, blue curves). In the deep ocean, salinity advection is controlled by the mean advection $\overline{q}(S_3' - S_4')$ (Figs. 12c, d, black curves), while the perturbation advection $q'(\overline{S_3} - \overline{S_4})$ (Figs. 12c, d, red curves) is nearly zero because $\overline{S_3} \approx \overline{S_4}$. The positive (negative) correlation between the perturbation (mean) advection and AMOC in our coupled model is also consistent with other relevant theoretical studies (e.g., Griffies and Tziperman 1995; Rivin and Tziperman 1997).

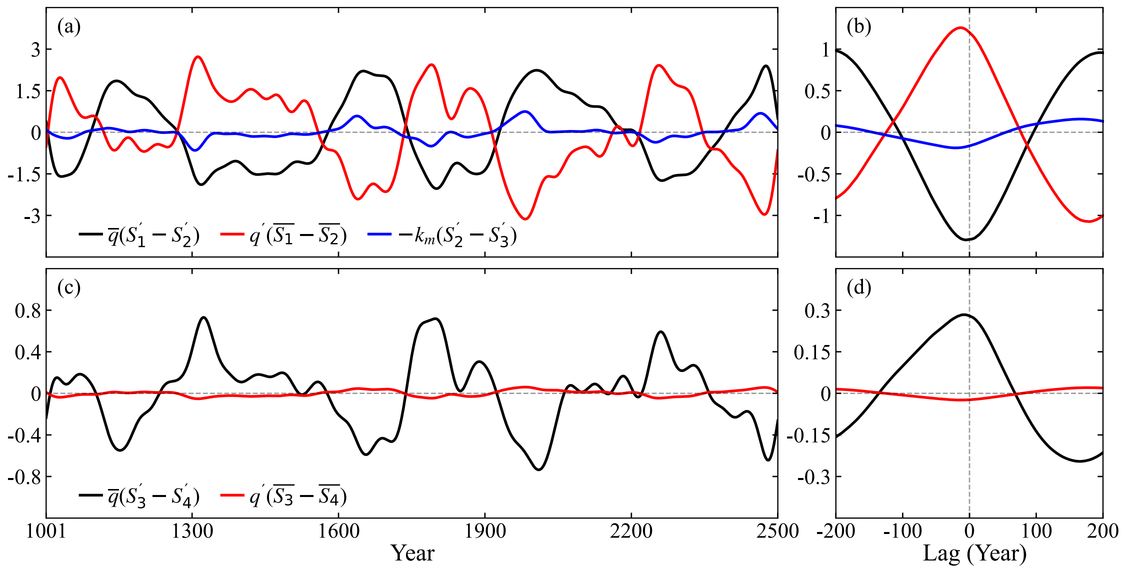

FIG. 12. (a) Time series for terms on the right-hand side of Eq. (A2), and (b) their lead/lag regression coefficients on the AMOC LFC1. (c) Time series for $\overline{q}(S_3' - S_4')$ and $q'\left(\overline{S_3} - \overline{S_4}\right)$, and (d) their lead/lag regression coefficients on the AMOC LFC1. Units for all curves are $Sv \cdot psu$. Negative lag means the AMOC LFC1 lags the salinity advection (units: year). Details on the North Atlantic division and the terms can be found in the appendix.

6. Summary and discussion

An MCO of the AMOC is identified in our CESM1 control simulation, which is dominated by processes in the North Atlantic and can be quantitatively explained by the theoretical model in LY22. In the subpolar North Atlantic, variation of salinity anomaly dominates variation of density anomaly, resulting in the AMOC oscillation. The essence of the AMOC MCO is summarized schematically in Fig. 13. The most critical process driving the AMOC MCO is the meridional salinity advection through the perturbation circulation in the subtropical-subpolar upper ocean. The northward mean advection of salinity anomaly from the subtropical intermediate ocean and the vertical salinity transport in the subpolar ocean weaken the AMOC anomaly. Concurrent with the AMOC evolution, salinity anomalies circulate in the North Atlantic on a similar timescale. The LFCA also suggests that it is the AMOC MCO that leads to the multicentennial variabilities of the global buoyancy fields.

Therefore, the AMOC may act as a pacemaker for multicentennial variability of the Earth's climate system.

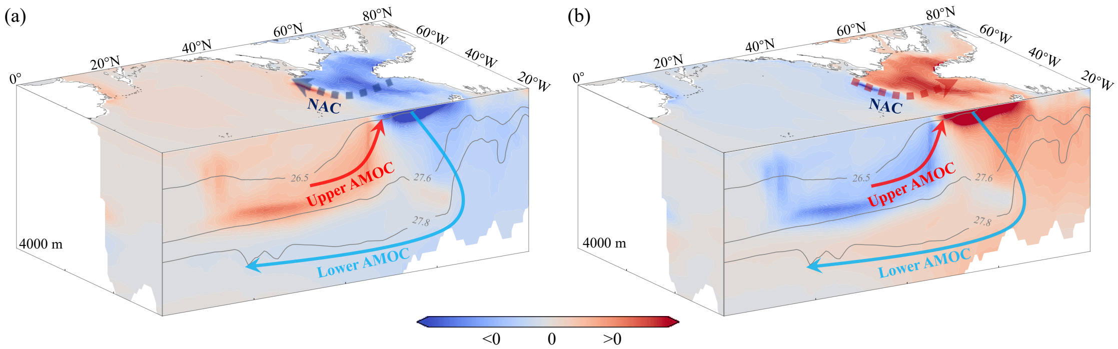

FIG. 13. Schematic diagrams showing oceanic states in the North Atlantic during (a) the negative phase and (b) the positive phase of the AMOC MCO. Dashed thick arrows represent changes of the NAC in the upper ocean. Solid red and blue arrows represent the upper and lower branches of the mean AMOC, respectively. (a) shows that when the AMOC is in the weak phase, the subpolar negative salinity anomaly is enhanced by the reduced NAC (dashed blue arrow) and, at the same time, weakened by the northward-upward mean advection of salinity anomaly in the intermediate ocean through the upper AMOC (solid red arrow) and downward-southward mean advection through the lower AMOC (solid blue arrow). (b) shows the opposite state to (a).

Our coupled model results suggest that the AMOC MCO is dominated by internal ocean dynamics in the North Atlantic. This conclusion is supported by several facts: (i) the AMOC LFP1 is very weak in the upper ocean and the wind-driven circulation is almost masked out by the LFCA, (ii) the center of the AMOC LFP1 is deeper than that of the climatological AMOC, (iii) the mean advection of salinity anomaly in the intermediate ocean affects the AMOC MCO more than that in the upper ocean, and (iv) the contribution of surface virtual salinity flux to the subpolar salinity anomaly is negligible. Therefore, the low-frequency variability has to be more closely related to deep ocean dynamics. This is different from the centennial-scale AMOC variabilities in previous studies such as Vellinga and Wu (2004), where the air-sea interaction in the tropical-subtropical region was emphasized as the dominant process.

The modeled AMOC MCO supports the theoretical study in LY22. In our current study, the South Atlantic is likely a sink rather than a source of salinity anomalies for the NADW formation. The Southern Ocean is not responsible for the AMOC MCO. Contribution from the Arctic Ocean to the AMOC MCO can also be neglected. One major significance of this study is the "North Atlantic origin" of the AMOC MCO we have identified, supporting the single-hemisphere theory in LY22. Salinity anomalies from the Arctic Ocean and Southern Ocean have been suggested as the drivers of multicentennial AMOC variability, both in lower-complexity model (Mikolajewicz and Maier-Reimer

1990; Mehling et al. 2022) and higher-complexity model (Jiang et al., 2021). Clear propagation of salinity anomalies from the Arctic Ocean or Southern Ocean is seen under their paradigms. However, in our CESM1 results, salinity anomaly in the upper level of the Arctic Ocean is much weaker than that of the subpolar convection region (Fig. 5a). In the intermediate ocean (Figs. 4d-f), there emerges a clear northward propagation of salinity anomaly from the subpolar region, suggesting that the Arctic Ocean is likely to be affected by, instead of affecting, the NADW formation. Since the ocean component we employed (POP2) differs from that used in the previous related studies, it is possible that the location of the most dominant processes can be related to the ocean model employed. Therefore, processes outside the North Atlantic cannot be deemed as completely effectless.

Timescale of the AMOC MCO can be closely related to its dominant processes. The essence for the "Arctic Ocean origin" paradigm is the sea ice-induced freshwater exchange at the surface while their periods are less than 200 years. With a similar mechanism, Jungclaus et al. (2005) found an AMOC oscillation with an even shorter period (70-80 years). Moreover, the centennial AMOC oscillation in Vellinga and Wu (2004) is dominated by the air-sea interaction, which is also a surface process. On the other hand, our "North Atlantic origin" and the "Southern Ocean origin" paradigms involve deep ocean processes, which should be responsible for their longer periods (>300 years). Mikolajewicz and Maier-Reimer (1990) also found a 320-year AMOC oscillation dominated by the deep convection in the Southern Ocean, although the model they used is an ocean-only model.

In this paper, we tried to demonstrate the liability of the North Atlantic-originated AMOC MCO through inter-verification between coupled and theoretical models. We feel that this mode will be more convincing if it can be verified by other coupled models, or by 2-D and 3-D models with complexities between that of our current study and LY22. Since the lower-complexity models have been shown to be capable of simulating AMOC MCOs (Mysak et al. 1993; Winton and Sarachik 1993; Drijfhout et al. 1996; Raa and Dijkstra 2003), it is likely that the "North Atlantic origin" paradigm can also be captured by certain lower-complexity models. However, the most powerful verification of this mode should be direct observations that are unfortunately unavailable in the foreseeable future. Since the internally driven AMOC MCO could have been a background of the anthropogenic centennial climate change, more studies on its mechanism should contribute to our understanding of the ongoing climate change.

Acknowledgements.

This research is jointly supported by the NSF of China (Nos. 42230403, 42288101, and 41725021) and by the foundation at the Shanghai Frontiers Science Centre of Atmosphere-Ocean Interaction of Fudan University. Prof. Q. Zhang acknowledges supports from Swedish Research Council (2022-03129).

Data Availability Statement.

All data used in this study are available upon request.

APPENDIX

A conceptual 4-box ocean model is used to explain the mechanism of the AMOC MCO in the coupled model. This box model has been used in Li and Yang (2022) and Yang et al. (2023) for theoretical studies of the AMOC multicentennial eigenmode. Following the box model (Fig. A1), the North Atlantic in our coupled model is also divided into four boxes. Boxes 1 and 4 are for tropical ocean spanning 0°-45°N, with box 1 covering 0-1000 m and box 4, 1000-4000 m. Boxes 2 and 3 are for subpolar ocean spanning 45°-70°N, with box 2 covering 0-1000 m and box 3, 1000-4000 m. In the box model, climatological (anomalous) salinities of boxes 1-4 are represented by $\overline{S_1}$ (S_1'), $\overline{S_2}$ (S_2'), $\overline{S_3}$ (S_3'), and $\overline{S_4}$ (S_4'), respectively. Climatological (anomalous) AMOC is represented by $\overline{q}$ (q'). Only salinity variation is considered here. The linearized salinity equations for the four boxes are:

$$V_1\dot{S}_1' = q'(\overline{S_4} - \overline{S_1}) + \overline{q}(S_4' - S_1') \tag{A1}$$

$$V_2\dot{S}_2' = q'\left(\overline{S_1} - \overline{S_2}\right) + \overline{q}(S_1' - S_2') - k_m(S_2' - S_3') \tag{A2}$$

$$V_3\dot{S}_3' = \overline{q}(S_2' - S_3') + k_m(S_2' - S_3') \tag{A3}$$

$$V_4\dot{S}_4' = \overline{q}(S_3' - S_4') \tag{A4}$$

where V_1, V_2, V_3, and V_4 are the volumes of boxes 1-4, respectively. Parameterization of q' was illustrated in LY22. k_m is a vertical mixing coefficient parameterized as $\kappa q'^2$, with κ = 10^{-5} m^{-3} s. The exact value of κ does not affect the oscillation period. Details on how k_m is determined can be found in LY22, which is based on Figs. 1g and 1h, that is, a strong Eulerian-mean AMOC is associated with a weak eddy-induced AMOC and vice versa.

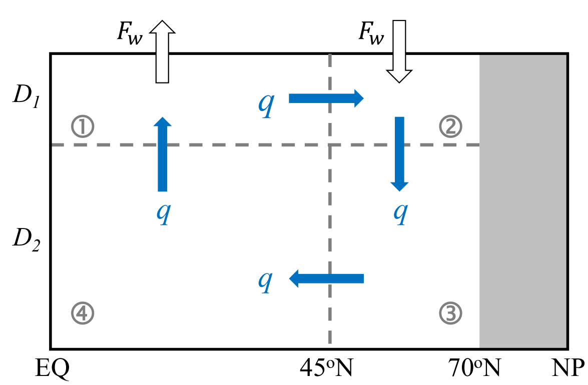

FIG. A1. Schematic of the 4-box ocean model. Ocean boxes are denoted by ①, ②, ③, and ④. Boxes 1 and 4 represent the upper and deeper layers of the tropical ocean, respectively; boxes 2 and 3, of the upper and deeper subpolar oceans, respectively. D_1 and D_2 are the depths of the upper and deeper boxes, respectively. F_w is the net freshwater flux out of (into) the tropical (subpolar) surface ocean. q represents the AMOC. This figure is reproduced from LY22.

As suggested in LY22, the mean (perturbation) advection process weakens (enhances) the anomalies of the subpolar upper salinity and thus the AMOC. However, the system is completely linear, and nonlinearity is needed to realize a self-sustained oscillation, which can take the form of an enhanced subpolar vertical mixing. Take the salinity anomaly in the subpolar upper ocean (box 2) as an example, the mean advection, perturbation advection, and enhanced vertical mixing are represented by $\overline{q}(S_1' - S_2')$, $q'\left(\overline{S_1} - \overline{S_2}\right)$, and $-k_m(S_2' - S_3')$, respectively.

Neglecting the vertical mixing term, linear stability analysis on Eqs. (A1-A4) can produce eigenmodes of the system, including an oscillatory multicentennial eigenmode found and studied thoroughly in LY22. Based on the imaginary parts of this mode, a theoretical solution to its period can be approximated as follows,

$$T = 2\pi \sqrt{V_1(V_2 + V_3)}/\overline{q} \tag{A5}$$

which translates into a period of 335 years under the volumes and $\overline{q}$ given in section 5b, close to that of the AMOC LFC1.

REFERENCES

Askjaer, T. G., and Coauthors, 2022: Multi-centennial Holocene climate variability in proxy records and transient model simulations. *Quat. Sci. Rev.*, **296,** 20, https://doi.org/10.1016/j.quascirev.2022.107801.

Ayache, M., D. Swingedouw, Y. Mary, F. Eynaud, and C. Colin, 2018: Multi-centennial variability of the AMOC over the Holocene: A new reconstruction based on multiple proxy-derived SST records. *Global Planet. Change*, **170,** 172-189, https://doi.org/10.1016/j.gloplacha.2018.08.016.

Buckley, M. W., and J. Marshall, 2016: Observations, inferences, and mechanisms of the Atlantic Meridional Overturning Circulation: A review. *Rev. Geophys.*, **54,** 5-63, https://doi.org/10.1002/2015rg000493.

Chabaud, L., M. F. S. Goni, S. Desprat, and L. Rossignol, 2014: Land-sea climatic variability in the eastern North Atlantic subtropical region over the last 14,200 years: Atmospheric and oceanic processes at different timescales. *Holocene*, **24,** 787-797, https://doi.org/10.1177/0959683614530439.

Chapman, M. R., and N. J. Shackleton, 2000: Evidence of 550-year and 1000-year cyclicities in North Atlantic circulation patterns during the Holocene. *Holocene*, **10,** 287-291, https://doi.org/10.1191/095968300671253196.

Craig, A. P., M. Vertenstein, and R. Jacob, 2012: A new flexible coupler for earth system modeling developed for CCSM4 and CESM1. *Int. J. High Perform. Comput. Appl.*, **26,** 31-42, https://doi.org/10.1177/1094342011428141.

Delworth, T. L., and F. R. Zeng, 2012: Multicentennial variability of the Atlantic meridional overturning circulation and its climatic influence in a 4000 year simulation of the GFDL CM2.1 climate model. *Geophys. Res. Lett.*, **39**, https://doi.org/10.1029/2012gl052107.

Drijfhout, S., C. Heinze, M. Latif, and E. MaierReimer, 1996: Mean circulation and internal variability in an ocean primitive equation model. *J. Phys. Oceanogr.*, **26,** 559-580, https://doi.org/10.1175/1520-0485(1996)026<0559:MCAIVI>2.0.CO;2.

Fox-Kemper, B., and R. Ferrari, 2008: Parameterization of mixed layer eddies. Part II: Prognosis and impact. *J. Phys. Oceanogr.*, **38,** 1166-1179, https://doi.org/10.1175/2007jpo3788.1.

Fox-Kemper, B., R. Ferrari, and R. Hallberg, 2008: Parameterization of mixed layer eddies. Part I: Theory and diagnosis. *J. Phys. Oceanogr.*, **38,** 1145-1165, https://doi.org/10.1175/2007jpo3792.1.

Gent, P. R., and J. C. Mcwilliams, 1990: Isopycnal mixing in ocean circulation models. *J. Phys.*

Oceanogr., **20,** 150-155, https://doi.org/10.1175/1520-0485(1990)020<0150:IMIOCM>2.0.CO;2.

Griffies, S. M., and E. Tziperman, 1995: A linear thermohaline oscillator driven by stochastic atmospheric forcing. *J. Climate*, **8,** 2440-2453, https://doi.org/10.1175/1520-0442(1995)008<2440:ALTODB>2.0.CO;2.

Hall, I. R., G. G. Bianchi, and J. R. Evans, 2004: Centennial to millennial scale Holocene climate-deep water linkage in the North Atlantic. *Quat. Sci. Rev.*, **23,** 1529-1536, https://doi.org/10.1016/j.quascirev.2004.04.004.

Hughes, T. M. C., and A. J. Weaver, 1994: Multiple equilibria of an asymmetric two-basin ocean model. *J. Phys. Oceanogr.*, **24,** 619-637, https://doi.org/10.1175/1520-0485(1994)024<0619:MEOAAT>2.0.CO;2.

Hunke, E., and W. Lipscomb, 2010: The Los Alamos Sea Ice Model, documentation and software user's manual, version 4.1. Los Alamos National Laboratory Rep. LACC-06-012, 76 pp.

Jiang, W. M., G. Gastineau, and F. Codron, 2021: Multicentennial variability driven by salinity exchanges between the Atlantic and the Arctic Ocean in a coupled climate model. *J. Adv. Model. Earth Syst.*, **13,** e2020MS002366, https://doi.org/10.1029/2020MS002366.

Jungclaus, J. H., H. Haak, M. Latif, and U. Mikolajewicz, 2005: Arctic-North Atlantic interactions and multidecadal variability of the meridional overturning circulation. *J. Climate*, **18,** 4013-4031, https://doi.org/10.1175/Jcli3462.1.

Kim, J. H., and Coauthors, 2004: North Pacific and North Atlantic sea-surface temperature variability during the Holocene. *Quat. Sci. Rev.*, **23,** 2141-2154, https://doi.org/10.1016/j.quascirev.2004.08.010.

Lawrence, D. M., and Coauthors, 2011: Parameterization improvements and functional and structural advances in version 4 of the Community Land Model. *J. Adv. Model. Earth Syst.*, **3,** 27, https://doi.org/10.1029/2011ms000045.

Li, Y., and H. J. Yang, 2022: A theory for self-sustained multicentennial oscillation of the Atlantic meridional overturning circulation. *J. Climate*, **35,** 5883-5896, https://doi.org/10.1175/Jcli-D-21-0685.1.

Marotzke, J., and P. H. Stone, 1995: Atmospheric transports, the thermohaline circulation, and flux adjustments in a simple coupled model. *J. Phys. Oceanogr.*, **25,** 1350-1364, https://doi.org/10.1175/1520-0485(1995)025<1350:ATTTCA>2.0.CO;2.

Martin, T., W. Park, and M. Latif, 2013: Multi-centennial variability controlled by Southern Ocean convection in the Kiel Climate Model. *Climate Dyn.*, **40,** 2005-2022, https://doi.org/10.1007/s00382-012-1586-7.

——, 2015: Southern Ocean forcing of the North Atlantic at multi-centennial time scales in the Kiel Climate Model. *Deep-Sea Res. Part II-Top. Stud. Oceanogr.*, **114,** 39-48, https://doi.org/10.1016/j.dsr2.2014.01.018.

McCarthy, G. D., and Coauthors, 2015: Measuring the Atlantic meridional overturning circulation at 26 degrees N. *Prog. Oceanogr.*, **130,** 91-111, https://doi.org/10.1016/j.pocean.2014.10.006.

McCarthy, G. D., and Coauthors, 2020: Sustainable observations of the AMOC: Methodology and technology. *Rev. Geophys.*, **58,** 34, https://doi.org/10.1029/2019rg000654.

McDermott, F., D. P. Mattey, and C. Hawkesworth, 2001: Centennial-scale Holocene climate variability revealed by a high-resolution speleothem delta 18O record from SW Ireland. *Science*, **294,** 1328-1331, https://doi.org/10.1126/science.1063678.

Meccia, V. L., R. Fuentes-Franco, P. Davini, K. Bellomo, F. Fabiano, S. T. Yang, and J. von Hardenberg, 2022: Internal multi-centennial variability of the Atlantic meridional overturning circulation simulated by EC-Earth3. *Climate Dyn.***,** 18, https://doi.org/10.1007/s00382-022-06534-4.

Mehling, O., K. Bellomo, M. Angeloni, C. Pasquero, and J. von Hardenberg, 2022: High-latitude precipitation as a driver of multicentennial variability of the AMOC in a climate model of intermediate complexity. *Climate Dyn.***,** 16, https://doi.org/10.1007/s00382-022-06640-3.

Miettinen, A., D. Divine, N. Koc, F. Godtliebsen, and I. R. Hall, 2012: Multicentennial variability of the sea surface temperature gradient across the subpolar North Atlantic over the last 2.8 kyr. *J. Climate*, **25,** 4205-4219, https://doi.org/10.1175/Jcli-D-11-00581.1.

Mikolajewicz, U., and E. Maier-Reimer, 1990: Internal secular variability in an ocean general circulation model. *Climate Dyn.*, **4,** 145-156, https://doi.org/10.1007/bf00209518.

Mysak, L. A., T. F. Stocker, and F. Huang, 1993: Century-scale variability in a randomly forced, two-dimensional thermohaline ocean circulation model. *Climate Dyn.*, **8,** 103-116, https://doi.org/10.1007/bf00208091.

Nakamura, M., P. H. Stone, and J. Marotzke, 1994: Destabilization of the thermohaline circulation by atmospheric eddy transports. *J. Climate*, **7,** 1870-1882, https://doi.org/10.1175/1520-0442(1994)007<1870:DOTTCB>2.0.CO;2.

Neale, R. B., and Coauthors, 2010: Description of the Community Atmosphere Model (CAM 4.0). Technical Report NCAR/TN-485+STR, National Center for Atmospheric Research, Boulder, CO, 268.

Newby, P. E., B. N. Shuman, J. P. Donnelly, K. B. Karnauskas, and J. Marsicek, 2014: Centennial-to-millennial hydrologic trends and variability along the North Atlantic Coast, USA, during the Holocene. *Geophys. Res. Lett.*, **41,** 4300-4307, https://doi.org/10.1002/2014gl060183.

Nyberg, J., B. A. Malmgren, A. Kuijpers, and A. Winter, 2002: A centennial-scale variability of tropical North Atlantic surface hydrography during the late Holocene. *Palaeogeogr. Palaeocl. Palaeoecol.*, **183,** 25-41, https://doi.org/10.1016/S0031-0182(01)00446-1.

Oppo, D. W., J. F. McManus, and J. L. Cullen, 2003: Palaeo-oceanography: Deepwater variability in the Holocene epoch. *Nature*, **422,** 277, https://doi.org/10.1038/422277b.

Park, W., and M. Latif, 2008: Multidecadal and multicentennial variability of the meridional overturning circulation. *Geophys. Res. Lett.*, **35**, https://doi.org/10.1029/2008gl035779.

Raa, L. A. T., and H. A. Dijkstra, 2003: Modes of internal thermohaline variability in a single-hemispheric ocean basin. *J. Mar. Res.*, **61,** 491-516, https://doi.org/10.1357/002224003322384906.

Rivin, I., and E. Tziperman, 1997: Linear versus self-sustained interdecadal thermohaline variability in a coupled box model. *J. Phys. Oceanogr.*, **27,** 1216-1232, https://doi.org/10.1175/1520-0485(1997)027<1216:LVSSIT>2.0.CO;2.

Roquet, F., G. Madec, T. J. McDougall, and P. M. Barker, 2015: Accurate polynomial expressions for the density and specific volume of seawater using the TEOS-10 standard. *Ocean Modell.*, **90,** 29-43, https://doi.org/10.1016/j.ocemod.2015.04.002.

Scott, J. R., J. Marotzke, and P. H. Stone, 1999: Interhemispheric thermohaline circulation in a coupled box model. *J. Phys. Oceanogr.*, **29,** 351-365, https://doi.org/10.1175/1520-0485(1999)029<0351:ITCIAC>2.0.CO;2.

Sévellec, F., T. Huck, and M. Ben Jelloul, 2006: On the mechanism of centennial thermohaline oscillations. *J. Mar. Res.*, **64,** 355-392, https://doi.org/10.1357/002224006778189608.

Smith, R., and P. Gent, 2010: The Parallel Ocean Program (POP) reference manual. Los Alamos National Laboratory Tech. Rep. LAUR-10-01853, 140 pp.

Stommel, H., 1961: Thermohaline convection with two stable regimes of flow. *Tellus*, **13,** 224-230, https://doi.org/10.1111/j.2153-3490.1961.tb00079.x.

Thirumalai, K., T. M. Quinn, Y. Okumura, J. N. Richey, J. W. Partin, R. Z. Poore, and E. Moreno-Chamarro, 2018: Pronounced centennial-scale Atlantic Ocean climate variability correlated with Western Hemisphere hydroclimate. *Nat. Commun.*, **9,** 392, https://doi.org/10.1038/s41467-018-

02846-4.

Vellinga, M., and P. L. Wu, 2004: Low-latitude freshwater influence on centennial variability of the Atlantic thermohaline circulation. *J. Climate*, **17,** 4498-4511, https://doi.org/10.1175/3219.1.

Wanner, H., and Coauthors, 2008: Mid- to Late Holocene climate change: An overview. *Quat. Sci. Rev.*, **27,** 1791-1828, https://doi.org/10.1016/j.quascirev.2008.06.013.

Wills, R. C., T. Schneider, J. M. Wallace, D. S. Battisti, and D. L. Hartmann, 2018: Disentangling global warming, multidecadal variability, and El Niño in Pacific temperatures. *Geophys. Res. Lett.*, **45,** 2487-2496, https://doi.org/10.1002/2017gl076327.

Winton, M., and E. S. Sarachik, 1993: Thermohaline oscillations induced by strong steady salinity forcing of ocean general-circulation models. *J. Phys. Oceanogr.*, **23,** 1389-1410, https://doi.org/10.1175/1520-0485(1993)023<1389:TOIBSS>2.0.CO;2.

Yin, F. L., 1995: A mechanistic model of ocean interdecadal thermohaline oscillations. *J. Phys. Oceanogr.*, **25,** 3239-3246, https://doi.org/10.1175/1520-0485(1995)025<3239:AMMOOI>2.0.CO;2.